# Multisatellite determination of the relativistic electron phase space density at geosynchronous orbit: Methodology and results during geomagnetically quiet times

Y. Chen, R. H. W. Friedel, and G. D. Reeves

Los Alamos National Laboratory, Los Alamos, New Mexico, USA

T. G. Onsager

NOAA, Boulder, Colorado, USA

M. F. Thomsen

Los Alamos National Laboratory, Los Alamos, New Mexico, USA

[1] We develop and test a methodology to determine the relativistic electron phase space density distribution in the vicinity of geostationary orbit by making use of the pitch-angle resolved energetic electron data from three Los Alamos National Laboratory geosynchronous Synchronous Orbit Particle Analyzer instruments and magnetic field measurements from two GOES satellites. Owing to the Earth's dipole tilt and drift shell splitting for different pitch angles, each satellite samples a different range of Roederer $L^*$ throughout its orbit. We use existing empirical magnetic field models and the measured pitch-angle resolved electron spectra to determine the phase space density as a function of the three adiabatic invariants at each spacecraft. Comparing all satellite measurements provides a determination of the global phase space density gradient over the range $L^* \sim 6-7$. We investigate the sensitivity of this method to the choice of the magnetic field model and the fidelity of the instrument intercalibration in order to both understand and mitigate possible error sources. Results for magnetically quiet periods show that the radial slopes of the density distribution at low energy are positive, while at high energy the slopes are negative, which confirms the results from some earlier studies of this type. We further show that the observed gradients near geosynchronous are generally small, making them very sensitive to both calibration and magnetic field model choice. This paper lays the foundation for this method for future applications to disturbed periods and for future inclusion of additional satellite data.

**Citation:** Chen, Y., R. H. W. Friedel, G. D. Reeves, T. G. Onsager, and M. F. Thomsen (2005), Multisatellite determination of the relativistic electron phase space density at geosynchronous orbit: Methodology and results during geomagnetically quiet times, *J. Geophys. Res.*, *110*, A10210, doi:10.1029/2004JA010895.

## 1. Introduction

[2] Understanding the dynamics of energetic electrons (with kinetic energy >0.1 MeV) in the Earth's radiation belts is of both intense scientific interest and practical significance. It has been observed that radiation belts relativistic electron fluxes can change dramatically during geomagnetic storms: The fluxes drop out during the main phase and then recover and frequently can be enhanced to $10-100$ times the prestorm levels [e.g., *Reeves*, 1998]. Such intensive high-energy electrons can impact satellites in the near-Earth space and sometimes reach low enough altitudes so that they can cause severe health risks to astronauts onboard the International Space Station. Since these space assets are so important to the modern world, the prediction of this so-called ''space weather'' is a topic of increasing interest.

[3] During the past decades, a large amount of relativistic electron data covering a substantial range of space and time have been acquired by a number of satellites. Several competing mechanisms have been proposed for the radiation belt electrons dynamics [*Friedel et al.*, 2002] and some of them are able to reproduce observations under certain circumstances. All the ingredients are thus in place to perform a systematic analysis of electron data from multiple satellites so as to eventually help differentiate the acceleration, transport, and loss processes that make up the observed dynamics [*Reeves et al.*, 2003].

[4] While electron flux observations are a function of geographic position, pitch angle, and energy, a physical understanding of the dynamics requires an investigation of the electron phase space density (PSD) at fixed values of the

phase space coordinates (PSCs), which are the first adiabatic invariant μ, the second adiabatic invariant $K$, and the Roederer parameter $L*$ [Roederer, 1970] associated with the third adiabatic invariant Φ, respectively (definitions given in Appendix B). Using the PSD at fixed PSCs allows us to both track particles through the system and to identify regions and times when the adiabatic assumption breaks down (injection events, fast loss events), and therefore to automatically filter out the so-called "Dst effect" [Kim and Chan, 1997], which leads to electron flux changes that are only due to the variation of the magnetic field configuration, i.e., are adiabatic.

[5] Although using PSD at fixed PSCs is not a new idea, the calculation of it is still sporadic, isolated and event-specific [e.g., Selesnick and Blake, 1997; Selesnick et al., 1997; Hilmer et al., 2000; Green and Kivelson, 2004; Onsager et al., 2004] and conclusions drawn from those studies are far from final and at times contradictory. This is due to the errors that can be introduced from various sources when one performs the PSD at fixed PSCs calculation. For example, the performance of magnetic field model is critical in the evaluation of the second and third adiabatic invariants; in the case of studying particle data from multiple satellites (or instruments), errors from coarse intersatellite (or interinstrument) calibration can be tremendous. Therefore strategies to constrain these errors need to be developed.

[6] We present a new method to determine the electron PSD radial distribution in the vicinity of geosynchronous orbit by using electron flux data from the Los Alamos National Laboratory (LANL) geosynchronous satellites and using GOES magnetic field data as a check on the magnetic field model. This method exploits Liouville's theorem, which requires that the PSD at fixed PSCs be preserved by the adiabatic transport in the inner magnetosphere during quiet times. Thus given a reliable magnetic field model, it is a very sensitive test of the instrument intercalibration used. This paper is primarily concerned with developing this method and testing it in a quiet time period for which we can assume that an existing empirical model is reliable. Application of this method to active storm times along with a technique of using the GOES magnetic field data to optimize the choice of external magnetic field will be presented in a follow-up paper (Y. Chen et al., Multisatellite determination of the relativistic electron phase space density at the geosynchronous orbit: Application to geomagnetic storm times, manuscript in preparation for Journal of Geophysical Research, 2005, hereinafter referred to as Chen et al., manuscript in preparation, 2005).

[7] A description of the instrumentation and data is presented in section 2. Section 3 describes the methodology for calculating the PSD radial distribution from multiple geosynchronous satellites. Section 4 presents the application of our method to a typical magnetically quiet day. This is followed by a discussion of the results and an examination of errors in section 5 and conclusions in section 6.

## 2. Instrumentation and Data

[8] Each of the LANL geosynchronous satellites is equipped with a Synchronous Orbit Particle Analyzer (SOPA) [Belian et al., 1992; Reeves et al., 1997] that in

**Table 1.** Geographic Longitudes and Magnetic Latitudes of GOES and LANL GEO Satellites on 11 December 2002[a]

| Satellite | Geographic Longitude, deg | Magnetic Latitude, deg |
|---|---|---|
| LANL-97A | ~103E | ~−10 |
| 1991-080 | ~165W | ~0 |
| GOES-10 | ~136W | ~4.5 |
| GOES-8 | ~75W | ~10.5 |
| 1990-095 | ~38W | ~10 |

[a]The magnetic latitudes are calculated using the IGRF and the Olson and Pfitzer [1977] magnetic filed models.

one spin measures the full three-dimensional electron distribution from 50 keV to more than 1.5 MeV. As these satellites carry no magnetometer, we use an indirect measure of the local magnetic field direction that can be derived from the symmetries of the plasma distribution (see Appendix A) measured by the lower-energy Magnetospheric Plasma Analyzer (MPA) [Thomsen et al., 1996]. This enables us to sort the SOPA electron differential flux measurements with respect to energy and pitch angle. The data used in this study have 10-min time resolution and come from the central telescope, which covers the largest portion of pitch angle for most of the time. At present, the available SOPA pitch angle resolved data cover a time range from July 2002 to September 2003.

[9] The spinning twin-fluxgate magnetometer, located on a boom a few meters away from the main body of each GOES satellite provide the magnitude and direction of the local magnetic field. The instrument has a sampling rate of 0.512 s, a sensitivity of 0.1 nT, and a range of 1000 nT. The accuracy is about 1 nT level after temperature correction [Singer et al., 1996]. A series of GOES satellites have been launched since GOES-8 in 1994. Typically, two GOES satellites are operational at any one time. The data used in this paper are from GOES-8 and GOES-10 with 1-min resolution, from the Coordinated Data Analysis Web (CDAWeb) (http://cdaweb.gsfc.nasa.gov/).

[10] We focus on a geomagnetically quiet day in this paper, 11 December 2002. The geomagnetic indices on that day indicate it was very quiet with $Dst > -15$ nT and $Kp < 2$. Additionally, during the previous consecutive 7 days, the geomagnetic indices also remained fairly quiet, with $Dst > -40$ nT and $Kp < 4-$, indicating that this day was not in the wake of any major storm. Data from the next day, 12 December 2002, are also used in this paper. Both days are published by the International Service of Geomagnetic Indices (ISGI) (http://www.cetp.ipsl.fr/isgi/BULL_MENS/b02/dec0201.html) as the most magnetically quiet days during that month. Orbital details of the geosynchronous satellites used are given in Table 1.

## 3. Description of the Methodology and Phase Space Density Calculation

[11] The idea of calculating electron PSD distribution and its local radial gradient by using data from multiple geosynchronous satellites was first introduced by Onsager et al. [2004] and has been applied to the calculation of PSD from two GOES satellites during a magnetically quiet period. In that paper, Onsager et al. obtained an outward positive radial gradient for the given adiabatic invariants at

geostationary orbit. The *Onsager et al.* [2004] study suffers from the lack of pitch angle information and from the limited energy resolution in the GOES data, and the necessarily imperfect assumptions of the distributions can affect the gradient derived from two points given the small radial range covered. This paper builds on the ideas [*Onsager et al.*, 2004] but uses the energy resolution and angular information of data from the LANL GEO SOPA instruments.

[12] The method used here is based on two facts. The first is the existence of the tilt angle ($\sim11.4°$) between the Earth's dipole and spin axis, which allows geosynchronous satellites to be located on different magnetic latitudes and to therefore sample electrons on magnetic field lines with different equatorial radial distances [*Onsager et al.*, 2004], as depicted in Figure 1a. This leads to sampling of different $L^*$ values even in a pure dipolar magnetic field. The second fact is the drift shell splitting phenomenon [*Stone*, 1963; *Roederer*, 1970]. Owing to the contributions from various current systems, the real inner magnetospheric magnetic field is nondipolar, quite asymmetric at most times, and increasingly asymmetric at larger radial distances. For example, two electrons, one with $\sim80°$ pitch angle and the other $\sim30°$, both starting from the same point on the nightside of geosynchronous orbit as depicted in Figure 1b, will not coincide with each other in the dayside since they drift along shells enclosing different magnetic fluxes. This allows energy and angular resolved electron flux instruments to measure the electron PSD points distributed on a surface in the three dimensional phase space at any given time (Figure 1c). Since each pitch angle determines a pair of ($K$, $L^*$), the surface has the characteristic that one curve is obtained when the surface is projected onto the ($K$, $L^*$) plane. As consequences of both facts presented above, at the same point in time, for each GEO satellite we can calculate the PSD values over one surface in the phase space. For any pair of satellites, the surfaces may be totally separated, intersected, or exactly the same. Figure 1c shows the plot of two phase space surfaces sampled by a pair of GEO satellites at one time point, with the color of the mesh indicating the PSD values. Hence when two PSD points from two GEO satellites have the same PSCs (e.g., points on the black straight line $P_{c1}P_{c2}$ where two surfaces cross each other in Figure 1c), the two points can be used to test the intersatellite calibration and accuracy of the magnetic configuration due to Liouville's theorem; when two points have the same first and second adiabatic invariants but separated $L^*$ values (e.g., the points $P_{g1}$ and $P_{g2}$ in Figure 1c), the PSD gradient is calculable. Obviously, the more GEO satellites included, the better coverage in phase space and the greater the ability to calculate the phase space density radial gradient.

[13] Following the methodology described above, we first need to obtain the PSD distribution of each GEO satellite. The calculation of PSD distribution involves two parts: one is determining the corresponding PSCs and the other is transforming fluxes to PSD values. The electron flux, calculated from directly observed counts, is a function of energy $E$, local pitch angle $\alpha$, and satellite position $\vec{r}$. In order to convert the flux $j(E, \alpha, \vec{r})$ to density in phase space $f(\mu, K, L^*)$, we use arrays of ($\mu$, $\alpha$) as the input and follow the steps outlined below.

[14] After an appropriate magnetic field model is selected, for one pair of given ($\mu_0$, $\alpha_0$), first, the given local pitch angle $\alpha_0$ allows us to calculate $K_0$ and $L^*_0$ according to the definitions given in Appendix B. Second, from equation (B1) we can calculate the corresponding energy $E_0$ for the given 1st adiabatic invariant $\mu_0$ and the local pitch angle $\alpha_0$. Interpolating the data for a full pitch angle distribution, we have the flux $j_{ch}(E_{ch}, \alpha_0, \vec{r})$ for each energy channel. Then, following *Hilmer et al.* [2000], we can create a list of PSDs for all energy channels by

$$f_{ch} = \left\{ \frac{j_{ch}}{\langle p^2c^2 \rangle_{ch}} \left[ 1.66 \times 10^{-10} \right] \right\} \times 200.3, \qquad (1)$$

where $j_{ch}$ is the flux in unit $cm^{-2}sr^{-1}keV^{-1}$, the terms in braces are equation (4) of *Hilmer et al.* [2000], and the multiplying factor is required to transform the PSD from Hilmer et al.'s unit to the GEM (Geospace Environment Modeling) unit $(c/MeV/cm)^3$, where c is the speed of light in a vacuum, and the term in the denominator is defined for each energy channel as

$$\langle p^2c^2 \rangle_{ch} = \frac{1}{2} \left[ K^{ch}_{min} \left( K^{ch}_{min} + 2m_0c^2 \right) + K^{ch}_{max} \left( K^{ch}_{max} + 2m_0c^2 \right) \right], \quad (2)$$

where the $K^{ch}_{min}$ and $K^{ch}_{max}$ are the lower and upper limit of each energy channel in MeV, respectively, and $m_0c^2$ is the rest energy of an electron. We define the energy of each channel as

$$E_{ch} = \sqrt{K^{ch}_{min} \cdot K^{ch}_{max}} \qquad (3)$$

considering a falling electron energy spectrum (Appendix C). Finally, interpolating the list of PSDs $f_{ch}(E_{ch}, \alpha_0, \vec{r})$ for all energy channels, we obtain the PSD for $E_0$, which is $f(\mu_0, K_0, L^*_0)$ when combined with the PSC calculated. Carrying out the calculation for other pairs of ($\mu$, $\alpha$), we obtain combinations of phase space coordinates, shown as the mesh in Figure 1c, and the corresponding PSD values.

## 4. Results for Geomagnetically Quiet Times

[15] In this section we present some initial results for applying the method to a geomagnetically quiet time, to provide a baseline for the electron PSD radial distribution around geosynchronous orbit. In our calculations we use the IGRF (International Geomagnetic Reference Field) as the internal magnetic model, while for the external model we use the quiet Olson and Pfitzer model (OP77) [*Olson and Pfitzer*, 1977] and the dynamic Tsyganenko '96 model (T96) [*Tsyganenko*, 1995; *Tsyganenko and Stern*, 1996]. We use two models here, since previous studies [*Selesnick and Blake*, 2000; *Green and Kivelson*, 2004] have shown that the PSD calculation in the region of study is sensitive to the performance of the chosen external model(s) and since both these models generally perform well during quiet times in the inner magnetosphere [*Jordan*, 1994; *Pulkkinen*, 2001]. The solar wind dynamic pressure, y and z components of the interplanetary magnetic field, and the geomag-
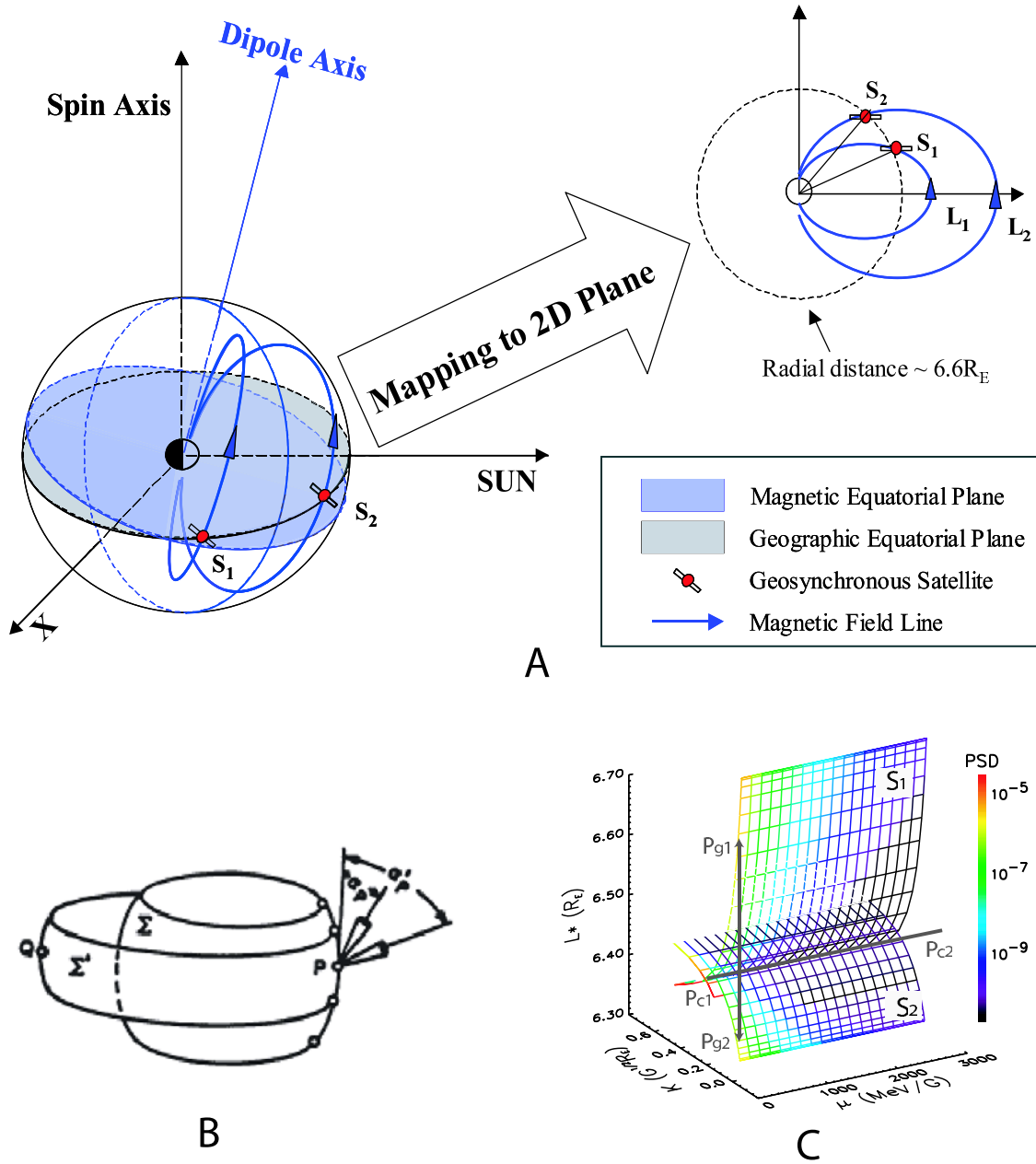
**Figure 1.** Conceptual illustration of our PSD methodology. (a) The three-dimensional (3-D) sketch shows that the dipole tilt angle puts satellites ($S_1$ and $S_2$) at different magnetic latitudes, and the mapped 2-D sketch shows how this allow GEO satellites to sample particles along different magnetic field lines; (b) Drift shell splitting phenomenon caused by different local pitch angles in nondipole field [*Roederer*, 1970]; (c) At any time, each satellite samples electrons distributed on a surface in the adiabatic phase space. Shown here are the two surfaces sampled by two GEO satellites ($S_1$ and $S_2$). The meshes on each surface are the phase space coordinates, and the color on each surface indicates the value of phase space density, with warm color corresponding to a large PSD value. The two surfaces intersect through the black straight line $P_{c1}P_{c2}$, points on which can be used for intercalibration, while points such as $P_{g1}$ and $P_{g2}$ which have the same first and second adiabatic invariants but different $L*$ can be used to derive the PSD radial gradient.
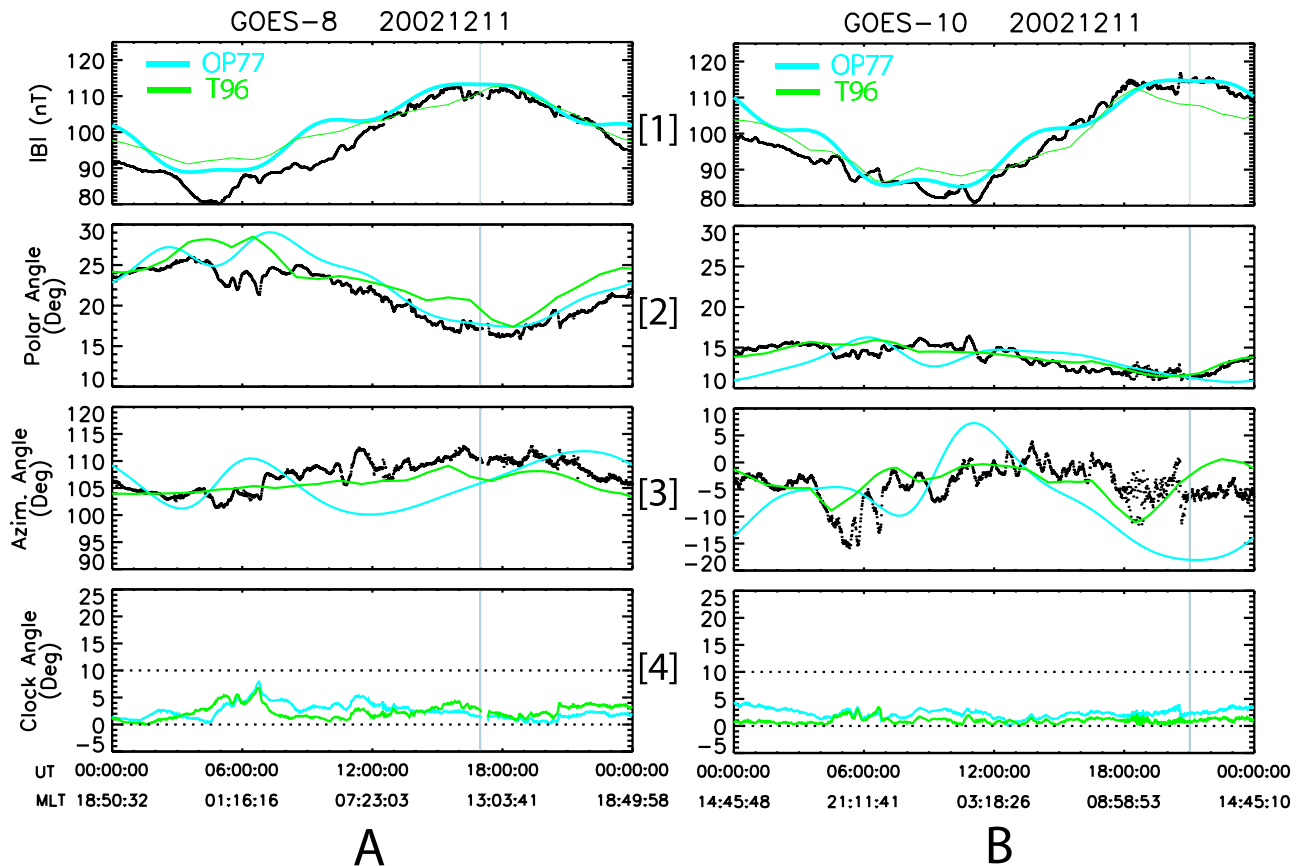
**Figure 2.** Comparison of model and data magnetic fields from (a) GOES-8 and (b) GOES-10, on 11 December 2002. The components are given in geographic coordinates for data (black), OP77 (aqua), and T96 (green). Panels in row 1 compare the magnitude, panels in row 2 compare the polar angle, panels in row 3 compare the azimuthal angle, and panels in row 4 show the angle between the two vectors (the "clock angle"). The time axes are the universal time (UT) and magnetic local time (MLT) labeled in the format of hh:mm:ss. The vertical line in each panel indicates the local noon.

netic index Dst required by the T96 model as input are obtained from the OMNIWeb (http://nssdc.gsfc.nasa.gov/omniweb/).

### 4.1. Magnetic Field Model Test

[16] Since the calculation of the PSD depends on the reliability of magnetic field, we evaluate the magnetic field models first. In Figure 2, magnetic vector measurements by GOES-8 and GOES-10 on 11 December 2002 are compared with output from the OP77 and T96 models in geographic coordinates. For GOES-8 an offset of 7 nT has been removed [*Tsyganenko et al.*, 2003]. Both models perform similarly. For GOES-10 which is located closer to the equatorial plane with magnetic latitude $\sim 5°$, both models give a better fit to the data, and the error in the magnitude is $<10\%$ (error in the average $<5$ nT) and the maximum angle deviation is $<5°$ (the average $<3°$) as shown in Figure 2b. For GOES-8 with a higher magnetic latitude of $\sim 10°$, the maximum error in magnitude is $\sim 15\%$ and the maximum angle $\sim 8°$, as shown in Figure 2a. In the case of GOES-8, both models perform better on the dayside than nightside, while for GOES-10 this is not so obvious. T96 gives a slightly better directional fit for GOES-10.

### 4.2. Magnetic Field Direction Test

[17] Our accuracy of transforming flux to PSD at constant PSCs relies on the accuracy of the pitch angle distribution that is obtained indirectly in this study. Figure 3 compares the magnetic field directions from models with the ones derived from each LANL GEO MPA measurement (*Thomsen et al.* [1996] or refer to Appendix A). Although fluctuations exist in the "clock angle" (the angle between model and data vectors) distribution for each satellite, the maximum angle deviation is less than $12°$ (average $<5°$) for each satellite. This provides us with confidence in the pitch angle differential flux from obtained from SOPA data.

### 4.3. Geosynchronous Electron PSD at Constant PSCs

[18] Having confirmed the fidelity of the magnetic field model and the pitch angle distribution, we now calculate the electron PSD at constant PSCs throughout the day for each satellite, following the steps described in section 3. The results are first presented as a function of time in Figure 4, which compares the PSD distributions against several variables and shows distinct local time features in the distributions.
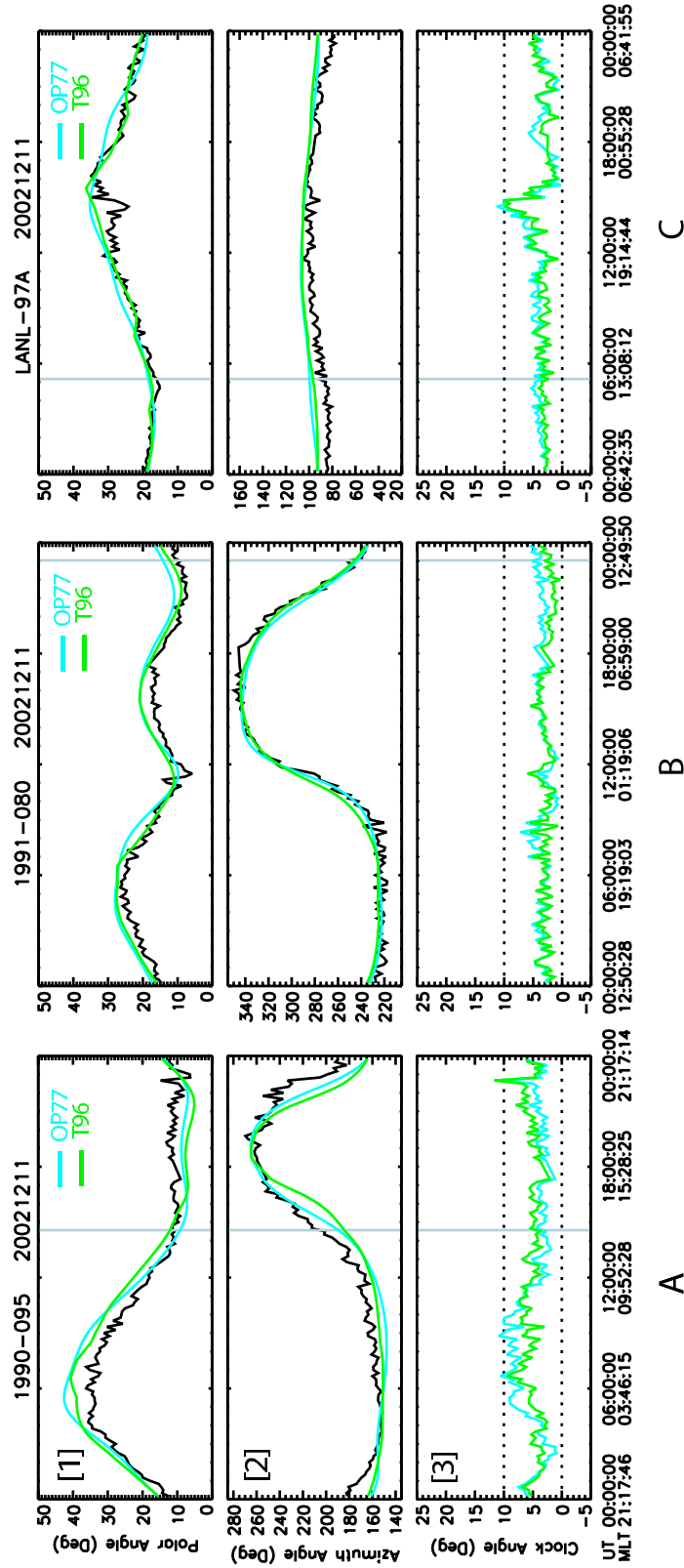
**Figure 3.** Magnetic field directions, derived from measurements by MPA onboard three LANL GEO satellites on 11 December 2002, compared with the output of the OP77 and T96 models. For (a) 1990-095, (b) 1991-080, and (c) LANL97A, the derived magnetic field direction is in black the output from OP77 in aqua and from T96 in green. Panels in row 1 compare the polar angles, panels in row 2 compare the azimuthal angle, and panels in row 3 compare the "clock angle" (the angle between model and data vectors). The components are given in geographic coordinates. The vertical line in each panel indicates local noon.
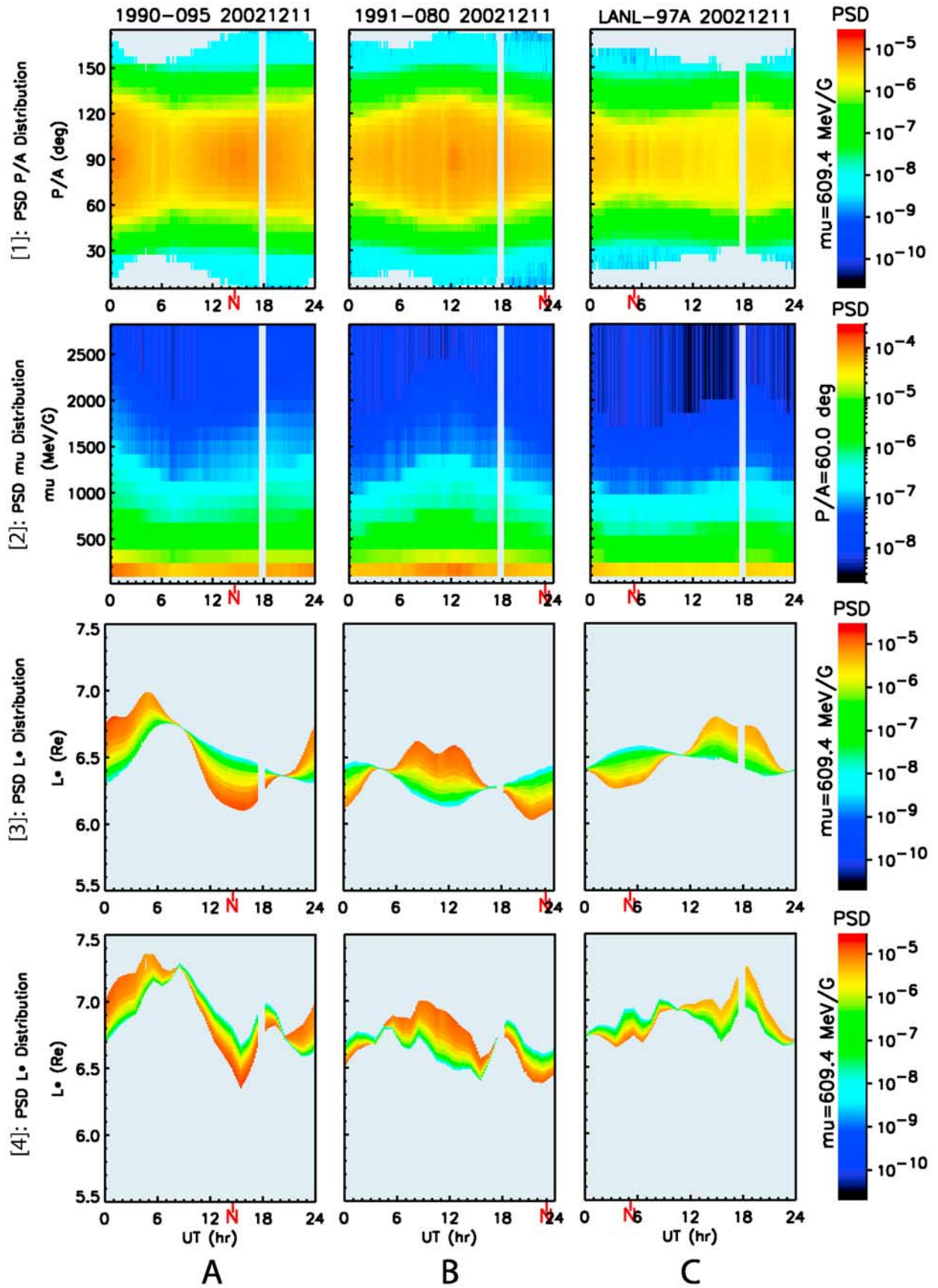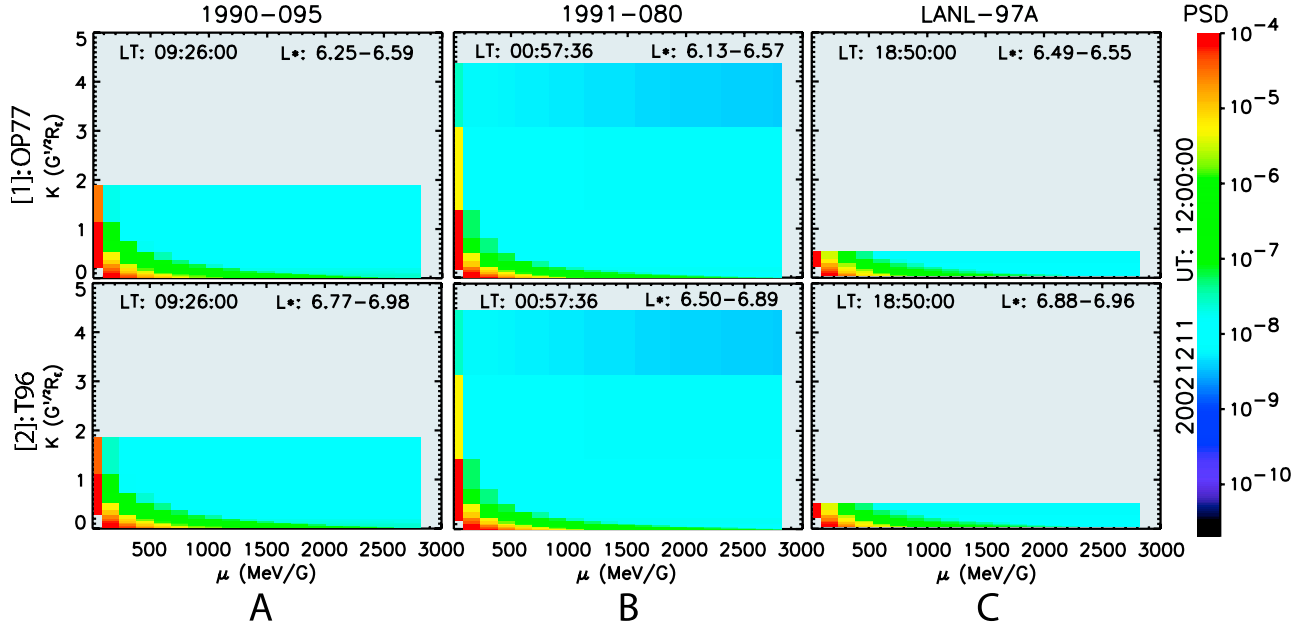
**Figure 4**

**Figure 5.** Snapshots of the PSD distributions versus ($\mu$, $K$) for (a) 1990-095, (b) 1991-080, and (c) LANL97A on 11 December 2002. Panel 1 shows the PSD calculated using the OP77 model and panel 2 for the T96 model. The range of corresponding $L^*$ values and the local times are indicated in each plot.

[19] The pitch angle distributions in row 1 of Figure 4 (with $\mu$ = 609.4 MeV/G, hence energies $\gtrsim$400 keV) are symmetrical around 90° as expected. More electrons distribute around 90° near local noon than midnight. This is mainly caused by the shell splitting effect in the presence of an azimuthally asymmetric magnetic field, giving a "pancake" pitch angle distribution (i.e., peaking at 90° pitch angle) at noon and a "cigar" (i.e., peaking at 0°/180° pitch angle) shaped distribution at midnight [*Baker et al.*, 1978]. This gives us further confidence in the fidelity of determining the magnetic field direction (Appendix A).

[20] While the distributions in row 1 of Figure 4 show differences in terms of universal time for three satellites, their local time features are very similar during this quiet day, except for the differences due to magnetic latitude. This is also true for the other results in Figure 4. In row 2 of Figure 4, the PSD versus $\mu$ distributions are given for a fixed pitch angle of 60°, and for each $\mu$ the PSD always reaches its minimum value around local noon since the magnetic field is compressed on the dayside.

[21] Drift shell splitting makes $L^*$ a distribution, instead of only one point, at any time and the $L^*$ corresponding to 90° pitch angle reaches a minimum around noon and a maximum at midnight, as shown by row 4 of Figure 4. It should be noted that though the PSD distribution with respect to $L^*$ sometimes shows larger PSD with larger (smaller) $L^*$ (e.g., in the first panel in row 3 of Figure 4, PSD value has red

color with $L^* \sim 7R_E(6.1R_E)$ when UT = 5 hours (16 hours), this does not necessarily mean a positive (negative) radial gradient since at a fixed time point each $L^*$ corresponds to a different $K$ as shown in Figure 1c. In other words, strictly speaking, at a given instant one can not obtain the radial PSD radial gradient using only one satellite.

[22] All the above results come from the OP77 model, and changing to the T96 model does not produce significant changes except for the PSD versus $L^*$ distribution, as shown in row 4 of Figure 4. Clearly, the T96 model shifts the $L^*$ range up almost $0.5R_E$ on average and shows more structure caused by the changing solar wind conditions, but other than that, compared with row 3 of Figure 4, the overall temporal profiles are almost the same.

[23] As mentioned in the introduction, the advantage of studying PSD is that the adiabatic effects (Dst effects) can be removed if electrons are traced at constant PSCs. This can be demonstrated by showing the PSD distributions as a function of the adiabatic invariants, as shown in Figure 5, which is a snapshot of the distributions for the three GEO satellites at UT = 12 hours during this quiet day. Each panel shows the color coded PSD magnitude as a function of $\mu$ and $K$, covering a range of $L^*$ as indicated.

[24] Row 1 of Figure 5 uses the OP77 model for the calculation, and row 2 of Figure 5 uses T96. The PSD distributions are quite similar for all satellites, with larger PSD values for smaller $\mu$ and $K$. The main difference caused

---

**Figure 4.** The PSD distributions on 11 December 2002 for (a) 1990-095, (b) 1991-080, and (c) LANL97A. Panels in row 1 show the PSD pitch angle distribution for given $\mu$ = 609.4 MeV/G; panels in row 2 show PSD versus $\mu$ for given pitch angle 60°; panels in row 3 are PSD versus $L^*$ for given $\mu$ = 609.4 MeV/G. The PSD values in all above panels are based on the OP77 model, while panels in row 4 show the same distribution as for the panels in row 3 but T96 being used. The red capital "N" on the time axis of each panel indicates the local noon position of the satellite.
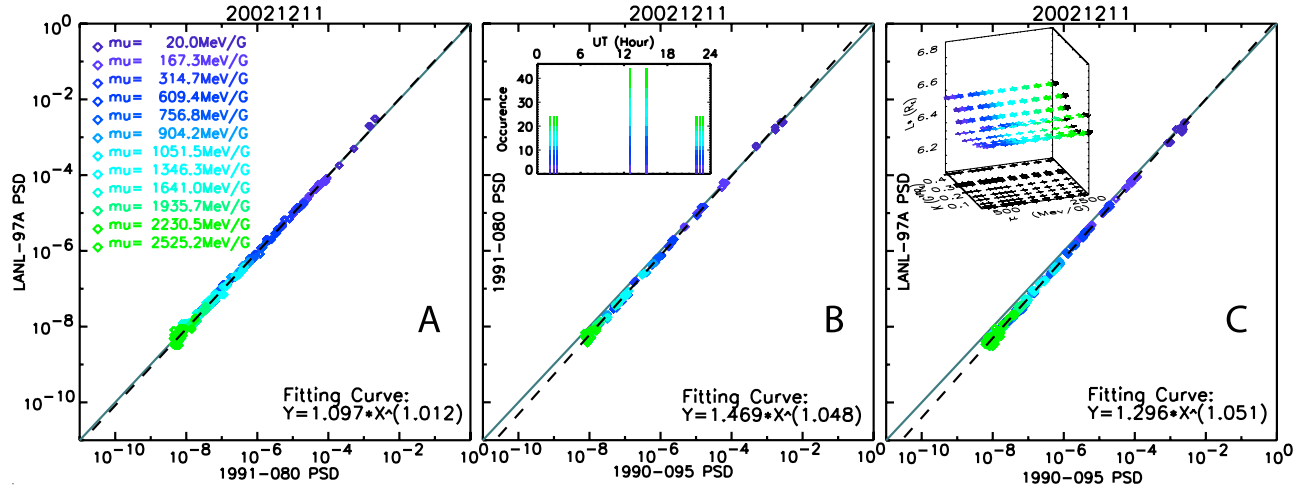
**Figure 6.** Cross-satellite calibration by comparing PSD at constant PSCs calculated by using the OP77 model. The solid diagonal of slope = 1 represents perfect intercalibration, and all PSD points are fitted to the dashed straight line using a least-squares fit. The resulting equation is shown in each plot. (a) Joint PSD points of 1990-095 and 1991-080. Different colors correspond to different $\mu$ values. (b) Joint PSD points of 1990-095 and LANL-97A. The small panel shows the occurrences of PSD points versus UT for the pair of satellites during the day. (c) Joint PSD points of 1991-095 and LANL-97A. In the 3-D panel in the up left corner, the plus signs (in colors) present the three phase space coordinates of the points, and the values can be read from the projections (in black) on the side walls.

by using two magnetic field models is the L* range, as we have seen in rows 3 and 4 of Figure 4. The panels in Figure 5 can be treated as the two-dimensional (2-D) planes mapped down from the 3-D surface in Figure 1c and the one-to-one mapping relationship between $K$ and $L*$ caused by drift shell splitting varies with satellite local time. For example, at this moment 1991-080 is located around midnight so that the $L*$ monotonically decreases with increasing $K$; thus its 3-D distribution is like the surface "$S_2$" in Figure 1c. For 1990-095 close to noon, $L*$ increases with $K$ and the sampled PSCs is more like the surface "$S_1$." For LANL-97A in the flank, the splitting phenomenon is the weakest and $L*$ spans over a narrow range at this position. This can also explain why the "radial gradient" appears positive some times and negative other times shown in Figures 4c and 4d. We have thus shown that the different location of each satellite allows us to sample in a different portion of phase space. This makes it feasible to obtain the radial gradient as illustrated in Figure 1c.

### 4.4. Detailed Satellite Intercalibrations

[25] Although the measurements from multiple satellites provide us with an opportunity to separate temporal effects from spatial ones, the problem of cross-satellite calibration has to be solved first to make the final results trustworthy. In this study, since only one kind of instrument (SOPA) is involved, the calibration is much easier. This has previously been done in a statistical way [*Boscher et al.*, 2003; *Friedel et al.*, 2005], where electron differential fluxes were averaged over 1-year period to remove the local time and other short term fluctuations and were then compared per energy channel between instruments, assuming all satellites should measure the same average counts. Coefficients provided by this statistic calibration enable us to transform the counts

measured by each instrument/satellite to fluxes. On the basis of the fluxes, a more rigorous intercalibration is proceeded in this study by comparing the PSD values between satellites at the same set of PSCs for a given time, which we call the "fine-tuned" calibration. Liouville's theorem requires PSD to be conserved at the same PSCs but different phases along the drifting shell in the absence of any losses or sources, which is a good assumption near geostationary orbit during magnetically quiet times. We perform this fine-tuned calibration for the whole of our quiet day (using the OP77 model) between our three spacecraft pairs, as shown in Figure 6.

[26] For any given satellite pair the diagonal line of slope = 1 indicates perfect intercalibration. Data are plotted here using the initial statistical calibration described above, which is already "close," giving minimal deviations from the diagonal for all satellite pairs. Detailed inspection of Figure 6 shows that the calibration between 1991-080 and LANL-97A is the best, while 1990-095 gives PSD values that are as much as 30% larger than those of LANL-97A for high-energy electrons, as shown in Figure 6c. Accordingly, choosing 1991-080 as the reference, we adjust the PSD values of 1990-080 and LANL-97A by using the fine-tuned calibration coefficients, shown as fitting equations in the figure.

[27] The small box in Figure 6b shows the universal time points when the PSD points are found for this pair of satellites, while for the other two pairs more PSD points indicate more time points. The 3-D box in Figure 6c shows the PSCs of the PSD points, and for each $K$ value there exist PSD points with different $\mu$ values forming a line, as predicted by the line $P_{c1}P_{c2}$ in Figure 1c. Therefore these calibration results are independent of time and pitch angles. The results stay almost the same when switching to the T96 model. These results show that fine-tuning the statistical
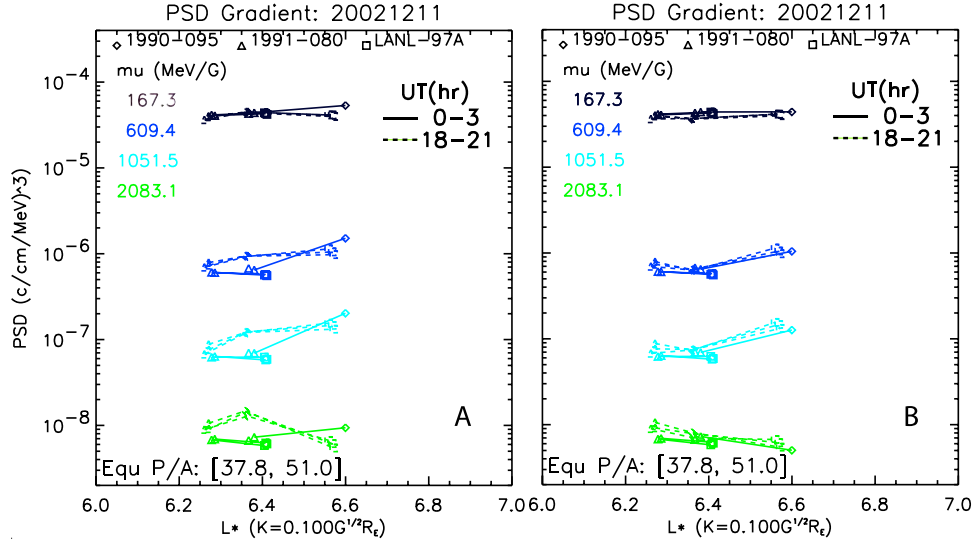
**Figure 7.** PSD radial distributions during UT = 0 ∼ 3 hours (solid lines) and UT = 18 ∼ 21 hours (dashed lines) on 11 December 2002. Different colors indicate different μ values. The lines connect data from our three geosynchronous satellites for the same time. (a) results without applying fine-tuned calibration, (b) results with fine-tuned calibrations. The OP77 model is used throughout.

calibrations of *Boscher et al.* [2003] and *Friedel et al.* [2005] is both feasible and meaningful.

[28] To further investigate the effects of calibration, we compare the PSD radial distributions during two 3-hour periods, as shown in Figure 7.

[29] With no fine-turned calibration applied, the gradients at the higher μ during UT = 0–3 hours have valleys in the middle while peaks in the same position are seen during UT = 18–21 hours, indicating persistent local time differences in the radial gradients, which could be interpreted as persistent losses (gains) of particles near $L^* = 6.4$ at UT = 0–3 hours (UT = 18–21 hours), in clear contradiction to Liouville's theorem as applied to this quiet day, where we would expect the same radial slope at all local times. In Figure 7b, after applying the fine-tuned calibration, the local time dependence of the radial slopes disappear, as is required by theory.

### 4.5. Radial PSD Gradients During Quiet Times

[30] One goal of this work is to calculate the PSD spatial distribution during magnetically quiet times, which can then serve as the baseline for a follow-up study of storm times. As a representative case, the full results for this quiet day, 11 December 2002, are presented in Figure 8, which covers several sets of adiabatic coordinates and also illustrates the effects of calibration and choice of magnetic field models.

[31] The panels in Figure 8 are plotted in the same way as those in Figure 7, except that all radial profiles throughout the day are shown. The length of the gray vertical bar on each point expresses the amount of uncertainty in the PSD by increasing/decreasing the local model magnetic field magnitude by 10%, to accommodate the model field/data variability shown in Figure 2 (assuming this causes no change in $K$ and $L^*$).

[32] As discussed in section 4.4, the radial distributions should be almost stationary during quiet magnetic condi-

tions, evolving slowly with time due to slow diffusion and loss processes (on timescales much larger than the time it takes for particles to drift from one spacecraft to another). The distributions at UT ∼ 12 hours on the following day, 12 December 2002, are shown in black for reference. The calculation is repeated by using T96 and Figure 8c presents the results. It is obvious that changing magnetic field model does not change the overall shape of the lines but shifts $L^*$ to a different range. Comparing Figures 8a and 8b, it can be seen that though each cluster of lines converge after applying calibration, the PSD values at larger $L^*$ decrease when compared to the profiles for the next day, thus decreasing the $L^*$ gradients with time.

[33] The radial gradients vary with adiabatic coordinates. For small $K = 0.06G^{1/2}R_E$, the gradients are positive for small μ, with the value of $(\partial f/\partial L^*)/f_{low}$ as high as $1.6/R_E$, and become negative at larger μ values, with the value of $(\partial f/\partial L^*)/f_{low}$ as low as $-2.5/R_E$. The same tendency is seen when $K$ increases to $0.1G^{1/2}R_E$ except the gradients start to become negative for smaller μ. This implies that the electron flux for high energy drops faster radially outward than that for low energy.

### 5. Discussion

[34] Being aware of the possible error sources and estimating and constraining them can improve the fidelity of the PSD calculation and minimize the chance of misleading results, e.g., the artificial peaks shown in Figure 7a. Generally speaking, the majority of errors are introduced by the poor performance of magnetic field models, inadequate interinstrument and/or intersatellite calibration, inaccurate assumption of particle pitch angle distribution, and the neglect of electric field effects. In this study of PSD in quiet times, we mainly focus on the effects of different magnetic field and fine-tuned intersatellite calibration. The
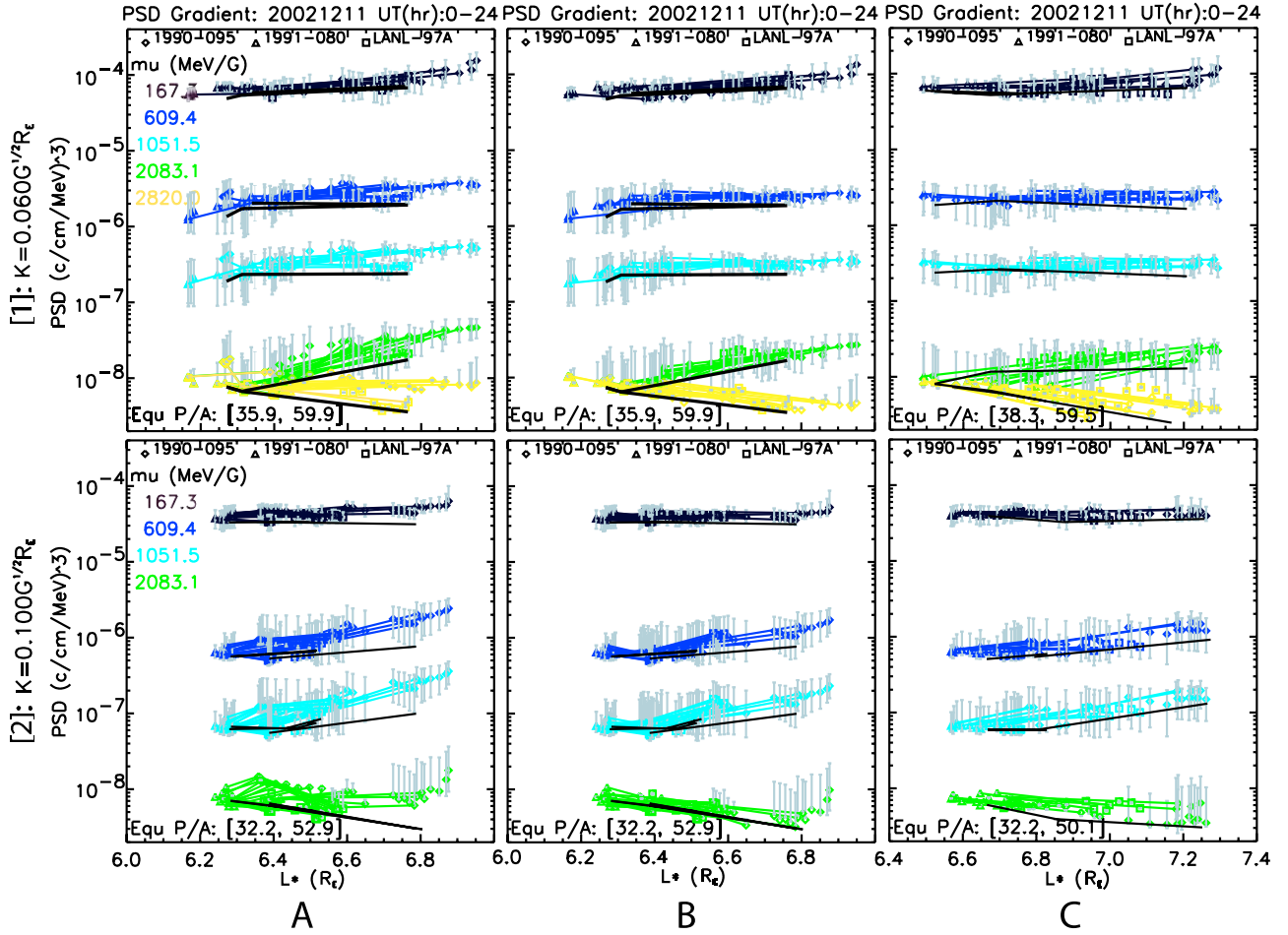
**Figure 8.** Overall PSD radial gradients on 11 December 2002. (a) Using the OP77 model, no fine-tuned calibrations, (b) using the OP77 model after applying fine-tuned calibrations and (c) using the T96 model after applying fine-tuned calibration. Panels in row 1 are for $K = 0.06G^{1/2}R_E$ and show the gradients at five $\mu$ values. Panels in row 2 are for $K = 0.1G^{1/2}R_E$ and show the gradients at four $\mu$ values. The PSD error bar is given in gray for each point by increasing/decreasing the local magnetic field magnitude by 10%. For the distribution of each $\mu$, a solid black curve is the corresponding radial gradient for the next day (12 December 2002) near 1200 UT.

LANL GEO data provides the electron pitch angle distribution and the effects of electric fields should be negligible for the study of electrons with energy larger than 100 keV [*Schulz and Lanzerotti*, 1974].

[35] The study of the electron dynamics in the frame of canonical momentum coordinates requires a good knowledge of magnetospheric magnetic field. Small deviation in the local $\vec{B}$ vectors can lead to error in the PSD value for a given $\mu$ value since the energy spectrum of electrons is generally not flat. Having a magnetic field instrument on board is better, as the associated uncertainties are much lower. When model fields are required, as is the case in this work, even the best matching efforts will lead to local errors, as we have seen from the gray error bar of each point in Figure 8. The PSD error can be as large as 100% with ±10% error in the field magnitude. However, we have no accurate way of getting at the errors due to the magnetic field model at each of our spacecrafts, since we simply do not know the real field. Thus the error bars in Figure 8 should be treated as a "worst case," not as an actual error.

[36] Another source of error that is hard to control and estimate comes from the large-scale magnetic field configuration, which is only available from models. From Figure 2 we can see that local measurements, even from multiple locations, sometimes can hardly differentiate the magnetic models. Not only are in situ measurements from satellites located appropriately at different radial distance and longitude and latitude needed, but also the PSD matching scheme should be involved to test the global configuration. Fortunately for this study, this problem is largely negligible since during quiet times the magnetospheric magnetic field is not stretched significantly and both the OP77 and T96 models have already been shown to perform well. Though the displacement in the $L^*$ values for the two models is not ignorable, it causes little problem to this work since that displacement is quite consistent through the whole quiet day. However, during disturbed times this problem turns out to be severe and special care should be taken to optimize magnetic field model (Chen et al., manuscript in preparation, 2005).

[37] We show that by fine-tuning the existing statistical calibration we can remove artificial PSD radial features (as shown in Figure 7), and demonstrate that delicate calibration is crucial in multiple satellite studies. Though the 30% overestimate of 1990-095 is not very large (which is quite natural considering the same SOPA instrument on board), we expect to see larger numbers when extending this fine-tuned calibration method to other satellites, such as between GEO and POLAR. Compared to the statistical calibration method, the fine-tuned calibration has at least two advantages: First, this approach can work for large satellite separations, as long as they can sample particles drifting on the same shell; and second, a long-duration joint data base is no longer needed (here the calibration is done within one day). The calibration should remain valid into disturbed times as long as there is no degradation in instrument performance. The only restriction is that this fine-tuned calibration has to be performed on data in geomagnetically quiet times so that the errors caused by magnetic field model can be minimized. It seems that a two-step calibration approach, first in the statistical way to acquire a coarse calibration, followed by detailed PSD comparisons at constant PSCs is the best method to achieve fine-tuned inter-calibration factors.

[38] Even though we cover only a small range of $L^*$ here, that the PSD radial distributions illustrated in Figure 8 show clearly different radial profiles for low- and high-energy electrons is consistent with the results of *Selesnick and Blake* [1997] and *Selesnick et al.* [1997]. According to the radial diffusion equation, the radial PSD distribution is determined by the radial diffusion coefficient, which is generally considered as a power function of radial distance, loss processes such as the pitch angle scattering, and a possible source from the tailward boundary. *Selesnick et al.* [1997] studied the distributions of two groups of electrons, one with $\mu = 1000$ MeV/G and the other $\mu = 6000$ MeV/G, both with $K = 0.10 G^{1/2} R_E$ and $L$ ranging from 3 to $6R_E$ during a 3-month magnetically quiet period. They successfully fit the diffusion model output with POLAR electron data and reproduced a peak of PSD at $L < 5R_E$ for electrons with high $\mu$ value. Since there is no external source from the large $L$ portion and loss dominates at the small $L$ portion, they saw decreasing PSD at both the higher and lower $L$ ends. This result is supported in our calculation by the decaying PSD of the electrons with $\mu = 2083$ MeV/G and $K = 0.1 G^{1/2} R_E$ with $L^* \sim 6-7$ on the next day 12 December 2002, shown in Figure 8. For the observed positive gradient for the electrons with low $\mu$, *Selesnick et al.* [1997] proposed a steady supply from the tail, assuming lower-energy electrons experience the same diffusion and loss processes. In our calculation, we obtained the same profiles for electrons with $\mu \leq 1051$ MeV/G and $K = 0.1 G^{1/2} R_E$, and the PSD values decrease slowly on the next day.

[39] We propose here the following possible scenario for explaining the observed radial profiles. First, we consider the spatial profiles for each episode of a particle injection: The flux at high energies can increases abruptly but is of short duration. This results in a narrow radial distribution. At low energies, increases can be as sharp but are generally of longer duration, resulting in a much wider radial distribution. Given the radial region we are sampling, which is near the trapping boundary for energetic electrons, we

have more of a chance to observe a positive gradient in $L^*$ for the low-energy electrons than for the high-energy electrons. Second, considering the temporal frequency of episodes of particle injections, particles can be injected intermittently and each injection event has different particle energy profiles. Particles at low energy are replenished so frequently that we can always see a fluctuating positive gradient as long as the mean time separation between injections is shorter than the mean loss time. Particles at very high energy have much less chance to refill; therefore we see a falling negative gradient over a long time period, and this is the case given by *Selesnick et al.* [1997]. Particles with moderate energy fall in between and can be seen to fluctuate in larger amplitude–positive gradient at one time but negative at another.

[40] Our results are inconsistent with those by *Onsager et al.* [2004], who derived a generally positive gradient for electrons at $\mu = 6000$ MeV/G and $K \sim 0$. However, the uncertainties introduced by the assumptions of energy and pitch angle distributions in that paper make it hard to compare with their results. Finally, the positive radial profiles of electron at low energy also emphasize that the differentiation of external and internal sources in storm times needs to trace the temporal evolution of radial profiles.

## 6. Conclusions

[41] We have presented a methodology used to determine the relativistic electron phase space density distribution in the vicinity of geostationary orbit by combining the electron data from three LANL geosynchronous SOPA instruments with magnetic field measurements from two GOES satellites. Exploiting the tilt of the magnetic equator with respect to the geographic equator and the drift shell splitting for different pitch angles for each satellite, we are able to derive the radial distribution of electron PSD in $L^* \sim 6-7R_E$. As a first test of the method and also to provide a reference for a follow-up study of storms periods, the calculation of electron PSD is processed for two magnetic quiet days.

[42] Magnetic field model selection and intersatellite calibration are the two major factors affecting precise PSD calculation. We use two empirical magnetic field models in this paper, and the error caused by imperfect magnetic field is estimated. It turns out that an appropriate choice of the magnetic field model plays an important role in the reliability of final results. Additionally, when studying data from multiple sources, the intersatellite calibration can be achieved or improved on by employing Liouville's theorem in magnetically quiet times so that artificial features in the PSD distribution can be avoided. Starting from LANL GEO, we can extend this calibration to other satellites such as POLAR and CLUSTER.

[43] Initial results for the magnetically quiet day demonstrate that the profile of electron phase space density radial distribution varies with energy, and this confirms the results from previous studies of this type. The slopes at low energy are positive or flat within the $L^*$ range covered here, while for high energy the slopes become negative. In both cases the PSDs continue dropping over time, which reflects the possibility that particles with different energy have different behavior in the injection events. Considering the positive

gradients of electrons at low energy, we cannot differentiate electron sources in disturbed times with a snapshot of radial distribution; instead we need to follow the changing PSD profiles in times.

[44] We will extend this method to the study of storm times in the future. Eventually, by including more satellites' data, the technique developed in this work is expected to contribute to a global data-assimilation based radiation belt model that simultaneously describes the field and particle distributions.

## Appendix A: Derivation of Local Magnetic Field Direction From LANL MPA Data

[45] As mentioned in section 2, there are no magnetometers on board LANL geosynchronous satellites, so an alternative method is needed to obtain the pitch angle distribution from plasma data. The method outlined below can derive local magnetic field direction from the measurements of thermal plasma by MPA [*Thomsen et al.*, 1996]. In the reference system of spacecraft with spin axis being z direction, due to the assumption of gyrotropy, from the count rate $(Cr_{ij})$ for 5-min averages in all polar/azimuthal $\theta/\phi$ bins, we form a $3 \times 3$ symmetric temperature matrix whose components are given as below:

$$T_{xx} = \Sigma_i \Sigma_j \left( Cr_{ij} \sin \theta_i \cos \phi_j \right) \sin \theta_i \cos \phi_j \quad (A1)$$

$$T_{xy} = \Sigma_i \Sigma_j \left( Cr_{ij} \sin \theta_i \cos \phi_j \right) \sin \theta_i \sin \phi_j \quad (A2)$$

$$T_{xz} = \Sigma_i \Sigma_j \left( Cr_{ij} \sin \theta_i \cos \phi_j \right) \cos \theta_i \quad (A3)$$

$$T_{yy} = \Sigma_i \Sigma_j \left( Cr_{ij} \sin \theta_i \sin \phi_j \right) \sin \theta_i \sin \phi_j \quad (A4)$$

$$T_{yx} = \Sigma_i \Sigma_j \left( Cr_{ij} \sin \theta_i \sin \phi_j \right) \cos \theta_i \quad (A5)$$

$$T_{zz} = \Sigma_i \Sigma_j \left( Cr_{ij} \cos \theta_i \right) \cos \theta_i \quad (A6)$$

Diagonalization of this matrix produces three eigenvalues and eigenvectors. We choose the direction of $\vec{B}$ to be equal to the eigenvector corresponding to the most unique eigenvalue. This method is successful as long as the distribution does not approach isotropy. When the electron distribution is isotropized (e.g., by injections), all eigenvalues become very similar and a unique eigenvalues cannot be identified so that the direction of magnetic field can no longer be derived in this way.

## Appendix B: Definition of the Three Phase Space Coordinates (PSCs)

[46] In this paper the phase space density is expressed in terms of three phase space momentum coordinates ($\mu$, $K$, $L^*$), which are associated with the three adiabatic invariants of the particle's motion. Here $\mu$ is the first invariant which

corresponds to the cyclotron movement of electron around a field line and is given by

$$\mu = \frac{p_\perp^2}{2m_0 B}, \quad (B1)$$

where $p_\perp$ is the relativistic momentum component perpendicular to the local magnetic vector, $m_0$ is the rest mass of electron, and $B$ is the local magnetic field magnitude. The second invariant has the original form of $J$ that is associated with the bounce movement of electron along a field line:

$$J = 2\sqrt{2m_0\mu} \int_{S_m}^{S'_m} \sqrt{B_m - B(s)} ds, \quad (B2)$$

where the subscript $m$ indicates the mirror point, and $B_m$ and $B(s)$ are the field strengths at the mirror point and point $s$, respectively. Here $ds$ is the distance along the field line. Since in $J$ the term outside of the integration sign is a constant, another form of the second adiabatic invariant is

$$K = \int_{S_m}^{S'_m} \sqrt{B_m - B(s)} ds \quad (B3)$$

which is a magnetic field related quantity with no reference to particles and is appropriate when radially following a particle population which breaks the third adiabatic invariant but preserves $K$ and $\mu$. Sometimes the integration

$$I = \int_{S_m^s}^{S_m^n} \left[ 1 - \frac{B(s)}{B_m} \right] ds \quad (B4)$$

is taken out of equation (3), and here $I$ is a purely field-geometric integral and sometimes can be very roughly interpreted as the length of field line along which the particle moves.

[47] The $L^*$, Roederer L parameter, is defined as the radial distance to the equatorial location where an electron crosses if all external magnetic fields were slowly turned off leaving only an internal dipole field [*Roederer*, 1970]. It is associated with the third adiabatic invariant in the form of
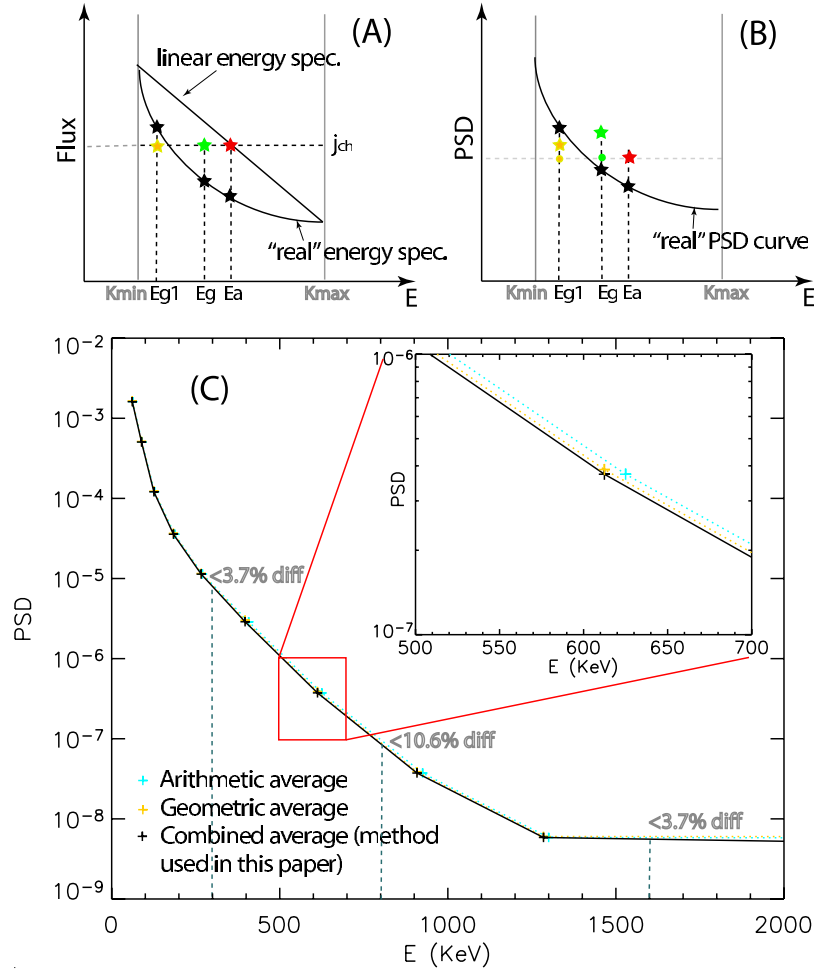
$$L^* = \frac{2\pi M}{|\Phi| R_E}, \quad (B5)$$

where $M$ is the Earth's dipole magnetic moment, $R_E$ is the Earth's radius, and $\Phi$ is the third invariant that is the magnetic flux through the electron's drifting shell and is given by

$$\Phi = \oint \vec{A} d\vec{x} \quad (B6)$$

or, equivalently,

$$\Phi = \int_S \vec{B} d\vec{S}, \quad (B7)$$

where $\vec{A}$ is the magnetic vector potential, $\vec{B}$ is the magnetic vector, $\vec{x}$ is the curve on the guiding center drift shell, and $S$ is cross section of the shell.

**Figure C1.** Effects of mean momentum and mean energy for SOPA energy channel(s). (a) Flux versus energy for one channel. Black stars on the "real" energy spectrum are the ultimate goal while color stars are what we can really achieve. (b) PSD versus energy. (c) The curves of PSD versus energy, calculated by three methods for all SOPA channel at one moment on a geomagnetically quiet day. Error percentages for interpolated PSDs at three energies are given.

[48] Besides the three momentum coordinates, a complete description of a particle's kinematical state requires three more positional coordinates, or so-called "phases," $(\phi_1, \phi_2, \phi_3)$ which correspond to the three adiabatic motions. Each combination of $(\mu, K, L^*; \phi_1, \phi_2, \phi_3)$ describes a point in the six-dimensional phase space. For a conserved system, Liouville's theorem demands a conserved distribution function along the path in phase space, which implies preserved PSD at constant $(\mu, K, L^*)$ with different $(\phi_1, \phi_2, \phi_3)$ so long as the adiabatic conditions are satisfied. For convenience, in this paper when we use the term "phase space coordinates," we refer to the momentum coordinates only, that is, the combination of $(\mu, K, L^*)$.

## Appendix C: Justification of the Equations (2) and (3)

[49] To achieve a $(f_{ch}, E_{ch})$ point for each SOPA energy channel, we choose to use geometrical mean momentum (equation (2)) and arithmetic mean energy (equation (3)). We made this choice based on two facts: one is that for each energy channel the flux $j_{ch}$ is derived from the counts by

assuming a linear energy spectrum; the other is the "real" energy spectrum is more likely to be exponential and vary with time and location. For a given $j_{ch}$, there are three possible choices.

[50] First is to use arithmetic mean momentum (as equation (2)) and arithmetic mean energy, which is given by

$$E_{ch} = \left(K_{min}^{ch} + K_{max}^{ch}\right)/2. \tag{C1}$$

The overly estimated $j_{ch}$ gives an overestimated PSD, indicated by the red star points at mean energy $E_a$ in Figures C1a and C1b.

[51] Second is to use geometrical mean momentum which is defined by

$$\langle p^2 c^2 \rangle_{ch} = \sqrt{K_{min}^{ch}\left(K_{min}^{ch} + 2m_0 c^2\right) \cdot K_{max}^{ch}\left(K_{max}^{ch} + 2m_0 c^2\right)} \tag{C2}$$

and geometrical mean energy (as equation (3)). There are two cases: one is $(K_{max} - K_{min})$ being small, which is the case for SOPA channels. In this case the mean energy $E_g$ is close to the $E_a$. The overly estimated flux $j_{ch}$ gives an

overestimated PSD, indicated by the green star points in Figures C1a and C1b; the other is $(K_{max} - K_{min})$ being large which leads to a mean energy $E_{g1}$ much smaller than $E_a$. The underestimated estimated flux $j_{ch}$ gives an underestimated PSD, indicated by the yellow star points in Figures C1a and C1b.

[52] The last, which is used in this paper, is to use the combined arithmetical mean momentum (as equation (2)) and geometric mean energy (as equation (3) which leads to either the green circle or the yellow circle in Figure C1b. Since narrow energy range is the general case of SOPA, we expect to obtain the green circle, which should be the best result. Of course, for other cases with wide energy range, this method will lead to a underestimated PSD (the yellow circle).

[53] A survey has been carried out to investigate the quantitative difference between PSD values obtained by above three methods, and results at one moment are shown in Figure C1c. It turns out that in quiet times, the error percentage is less than 11%.

# References

Baker, D., P. Higbie, E. W. Hones, and R. Belian (1978), High resolution energetic particle measurements at $6.6R_E$: 3. Low energy electron anisotropies and short term substorm predictions, *J. Geophys. Res.*, *83*, 4863–4868.

Belian, R., G. Gisler, T. Cayton, and R. Christensen (1992), High−z energetic particles at geosynchronous orbit during the great solar proton event series of October 1989, *J. Geophys. Res.*, *97*, 16,897–16,906.

Boscher, D., S. Bourdarie, R. Friedel, and R. Belian (2003), Model for the geostationary electron environment: POLE, *IEEE Trans. Nucl. Sci.*, *50*, 2278–2283.

Friedel, R., G. Reeves, and T. Obara (2002), Relativistic electron dynamics in the inner magnetosphere—A review, *J. Atmos. Solar Terr. Phys.*, *64*, 265.

Friedel, R., S. Bourdarie, and T. Cayton (2005), Intercalibration of magnetospheric energetic electron data, *Space Weather*, *3*, S09B04, doi:10.1029/2005SW000153.

Green, J., and M. Kivelson (2004), Relativistic electrons in the outer radiation belt: Differentiating between acceleration mechanisms, *J. Geophys. Res.*, *109*, A03213, doi:10.1029/2003JA010153.

Hilmer, R., G. Ginet, and T. Cayton (2000), Enhancement of equatorial energetic electron fluxes near $L = 4.2$ as a result of high speed solar wind streams, *J. Geophys. Res.*, *105*, 23,311–23,322.

Jordan, C. E. (1994), Empirical models of the magnetospheric magnetic field, *Rev. Geophys.*, *32*, 139–157.

Kim, H., and A. Chan (1997), Fully-adiabatic changes in storm-time relativistic electron fluxes, *J. Geophys. Res.*, *102*, 22,107–22,116.

Olson, W., and K. Pfitzer (1977), Magnetospheric magnetic field modeling, Tech. Rep., McDonnell Douglas Astronaut. Co., Huntington Beach, Calif.

Onsager, T., A. Chan, Y. Fei, S. Elkington, J. Green, and H. Singer (2004), The radial gradient of relativistic electrons at geosynchronous orbit, *J. Geophys. Res.*, *109*, A05221, doi:10.1029/2003JA010368.

Pulkkinen, T. (2001), How to address the accuracy of empirical magnetic field models, *Adv. Space Res.*, *28*, 1717–1726.

Reeves, G. (1998), Relativistic electrons and magnetic storms: 1992–1995, *Geophys. Res. Lett.*, *25*, 1817–1820.

Reeves, G., R. Belian, T. Cayton, M. Henderson, R. Christensen, P. McLachlan, and J. Ingraham (1997), Using los alamos geosynchronous energetic particle data in support of other missions, in *Satellite-Ground Based Coordination Source Book*, edited by M. Lockwood and H. Opgenoorth, pp. 263–272, Eur. Space Agency, Noordwijk, Netherlands.

Reeves, G. D., K. L. McAdams, R. H. W. Friedel, and T. P. O'Brien (2003), Acceleration and loss of relativistic electrons during geomagnetic storms, *Geophys. Res. Lett.*, *30*(10), 1529, doi:10.1029/2002GL016513.

Roederer, J. (1970), *Dynamics of Geomagnetically Trapped Radiation*, Springer, New York.

Schulz, M., and L. Lanzerotti (1974), *Particle Diffusion in the Radiation Belts*, Springer, New York.

Selesnick, R., and J. Blake (1997), Dynamics of the outer radiation belt, *Geophys. Res. Lett.*, *24*, 1346–1350.

Selesnick, R., and J. Blake (2000), On the source location of radiation belt relativistic electrons, *J. Geophys. Res.*, *105*, 2607–2624.

Selesnick, R., J. Blake, W. Kolasinski, and T. Fritz (1997), A quiescent state of 3 to 8 Mev radiation belt electrons, *Geophys. Res. Lett.*, *24*, 1343–1346.

Singer, H., L. Matheson, R. Grubb, and A. Bouwer (1996), Monitoring space weather with the GOES magnetometers, in *GOES-8 and Beyond*, vol. 2812, edited by E. Washwell, pp. 299–308, SPIE, Bellingham, Wash.

Stone, E. (1963), The physical significance and application of $L$, $B_0$ and $R_0$ to geomagnetically trapped particles, *J. Geophys. Res.*, *68*, 4157–4166.

Thomsen, M., D. McComas, G. Reeves, and L. Weiss (1996), An observational test of the Tsyganenko (T89a) model of the magnetospheric field, *J. Geophys. Res.*, *101*, 24,827–24,836.

Tsyganenko, M. (1995), Modeling the Earth's magnetospheric magnetic field confined within a realistic magnetopause, *J. Geophys. Res.*, *100*, 5599–5621.

Tsyganenko, M., and D. Stern (1996), Modeling the global magnetic field the large-scale birkeland current system, *J. Geophys. Res.*, *101*, 27,187–27,198.

Tsyganenko, M., H. Singer, and J. Kasper (2003), Storm-time distortion of the inner magnetosphere: How servere can it get?, *J. Geophys. Res.*, *108*(A5), 1209, doi:10.1029/2002JA009808.

————————————

Y. Chen, R. H. W. Friedel, G. D. Reeves, and M. F. Thomsen, Los Alamos National Laboratory, P.O. Box 1663, MS D466, Los Alamos, NM 87545, USA. (cheny@lanl.gov; rfriedel@lanl.gov; reeves@lanl.gov; mthomsen@lanl.gov)

T. G. Onsager, NOAA R/E/SE, 325 Broadway, Boulder, CO 80303, USA. (terry.onsager@noaa.gov)